Carbohydrate Polymers 316 (2023) 121058

Contents lists available at ScienceDirect

Carbohydrate Polymers

journal homepage: www.elsevier.com/locate/carbpol

Hydrophilic chitosan/graphene oxide composite sponge for rapid hemostasis and non-rebleeding removal

Fanglin Du [a], Wenjing A [a], Fang Liu [b], Bingxin Wu [a], Yichun Liu [a], Weitao Zheng [c], Wenli Feng [a], Guofeng Li [a,*], Xing Wang [a]

[a] State Key Laboratory of Organic-Inorganic Composites, Beijing Laboratory of Biomedical Materials, Beijing University of Chemical Technology, Beijing 100029, PR China

[b] Department of Oncology of Integrative Chinese and Western Medicine, China-Japan Friendship Hospital, Beijing 100029, China

[c] Hubei Provincial Key Laboratory of Industrial Microbiology, Sino-German Biomedical Center, National "111" Center for Cellular Regulation and Molecular Pharmaceutics, Hubei University of Technology, Wuhan 430068, Hubei Province, China

ARTICLE INFO

Chemical compounds studied in this article:
Chitosan (PubChem CID: 71853)
Graphite powders (PubChem CID: 5462310)
Sodium nitrate (PubChem CID: 24268)
Sulfuric acid (PubChem CID: 1118)
Hydrochloric acid (PubChem CID: 313)
Ammonium persulfate (PubChem CID: 62648)
Hydrogen peroxide (PubChem CID: 784)
Potassium permanganate (PubChem CID: 516875)
Methacrylic anhydride (PubChem CID: 12974)
N,N′-Methylenebisacrylamide (PubChem CID: 8041)

Keywords:
Hydrophilic hemostatic sponge
Graphene oxide
Rapid hemostasis
Anti-adhesion
Non-rebleeding removal

ABSTRACT

Hydrophilic hemostatic sponge plays an important role in trauma bleeding control because of its robust coagulant functions. However, its strong tissue adhesion can easily result in wound tear and rebleeding during removing the sponge. Herein, the design of a hydrophilic anti-adhesive chitosan/graphene oxide composite sponge (CSAG) that possesses stable mechanical strength, rapid liquid absorption and strong intrinsic/extrinsic coagulation stimulations, is reported. For one thing, CSAG exhibits outstanding hemostatic performance, which significantly outperforms two commercial hemostats in two *in vivo* serious bleeding models. For another, CSAG shows low tissue adhesion; its peeling force is approximately 79.3 % lower than the commercial gauze. Moreover, in the peeling process, CSAG triggers partial detachment of the blood scab, because of the exist of bubbles or cavities at the interface, allowing the CSAG to be easily and safely peeled off from the wound without rebleeding. This study opens new avenues in constructing anti-adhesive trauma hemostatic materials.

1. Introduction

Using hemostatic materials against massive hemorrhage is crucial for saving patients life (Guo, Dong, Liang, & Li, 2021; Wang, You, Dai, Tong, & Wu, 2020). The coagulation process assisted with hemostatic materials involves the contact between the materials and wound, the blood clot formation triggered by the materials and the stripping of the materials. The removal of the materials, however, frequently causes secondary bleeding accompanied by serious pain and a high infection risk (Li et al., 2019; Zhang et al., 2021a, b). To date, superhydrophobic coating on the material surface is a predominant strategy for achieving anti-adhesion, such as superhydrophobic polydimethylsiloxane/TiO_2 film (Liu et al., 2020), polytetrafluoroethylene/carbon nanofibers patch (Li et al., 2019), and beeswax/carbon nanofibers/kaolin gauze (Li, Niu, Zhao, Yap, & Li, 2021). The superhydrophobic surfaces are commonly blood repellent, preventing blood from entering materials (Jokinen, Kankuri, Hoshian, Franssila, & Ras, 2018). These hydrofuge hemostatic strategies, therefore, maximally supper the formation of scab/material composite that effectively avoids secondary bleeding. However, it should be noted that the non-contact between blood (in which coagulation factors and platelets are inside) and the materials sacrifice the coagulation stimulations induced by the materials (Li et al., 2019; Zhu et al., 2018); the trigger of the coagulation pathway mainly relies on the body itself. In this regard, the body will lose the ability of bleeding

* Corresponding author.
E-mail address: ligf@mail.buct.edu.cn (G. Li).

https://doi.org/10.1016/j.carbpol.2023.121058
Received 15 September 2022; Received in revised form 18 May 2023; Accepted 23 May 2023
Available online 27 May 2023

control in the case of severe hemorrhage, whilst the blood will overflow from the gap between the wound and the material, resulting in frequent hemostasis failure (Long et al., 2021; Moradi, Hadjesfandiari, Toosi, Kizhakkedathu, & Hatzikiriakos, 2016).

Comparatively, hydrophilic hemostatic materials are conducive to hemorrhage control. They can effectively stop bleeding by accumulating blood cells to form a thrombus and exerting a cascade response of coagulation (Fang et al., 2020; Liang et al., 2019; Wang et al., 2017). Previous studies revealed that a hydrophilic surface rather than a hydrophobic surface drives the formation of stable blood scabs, which is critical to sealing the wound and reducing blood loss (Ruhoff et al., 2021). However, hydrophilic hemostatic materials used as anti-adhesion materials are still in their infancy, and there are two facing challenges. i) A controversial obstacle is that hydrophilic materials easily absorb excess blood which would lead to the formation of the material/scab composite, subsequently resulting in secondary bleeding (Li et al., 2019; Long et al., 2021). But till now, there is currently no clear conclusion on the effect of the material/scab composite on secondary bleeding. The separation process of the hemostatic material from the blood scab has rarely been studied. ii) It should be noted that the tissue around the wound will have strong adhesion with the hydrophilic surface because of diverse non-covalent interactions such as hydrogen bond interaction and charge interaction (Hong et al., 2019; Song et al., 2021). For example, chitosan is a widely used hemostatic polysaccharide due to its excellent aggregation effect on blood cells (Deineka et al., 2021; Hu, Zhang, Lu, Li, & Li, 2018; Li et al., 2020b, b). But there is an inevitable strong adhesion between chitosan and tissue because of their charge interactions (Mati-Baouche et al., 2014). The adhesion strength of chitosan-based hemostatic hydrogels to porcine skin can be up to 68.5 kPa (Song et al., 2021), which is strong enough to tear the wound and destroy the blood scab, resulting in secondary bleeding. Therefore, the development of hydrophilic anti-adherent hemostatic materials is of great significance and challenging.

Graphene oxide (GO) is a two-dimensional carbon nanomaterial that has super-affinity with water (Gulzar et al., 2017; Reina et al., 2017; Zhang et al., 2020). Its three-dimensional porous sponges possess ultrafast liquid absorption ability (Nair, Wu, Jayaram, Grigorieva, & Geim, 2012; Quan et al., 2015; Yang et al., 2021). Furthermore, GO can evoke strong aggregatory response in platelets due to the oxygenated functional groups on its surface, which can promote the formation of blood clots (Kumari, Singh, Singh, Grácio, & Dash, 2014; Singh et al., 2011). According to reports, GO-based composites exhibit excellent biocompatibility (Depan, Girase, Shah, & Misra, 2011; Liao, Lin, Macosko, & Haynes, 2011), and show excellent hemostatic potential (Li et al., 2016; Li, Quan, Xu, Deng, & Wang, 2018a; Quan et al., 2016; Wu, Du, Wenjing, Li, & Wang, 2022). More importantly, the negatively charged GO has revealed charge repulsion with tissue (Liu, Zhang, He, Zhao, & Bai, 2010), and their two-dimensional lamellar structure increases the roughness of its composites (Lu et al., 2018; Uysal, Akbulut, Tokur, Algül, & Çetinkaya, 2016). These properties are in favor of reducing adhesion force at the material/tissue interface and facilitating the non-bleeding separation of the composites from the wound. Therefore, it could be speculated that GO would be a potential material to improve the hemostatic properties of the composites and impart their anti-adhesive properties.

Herein, a series of hydrophilic chitosan/GO composite sponges (CSAGs) was constructed *via* a thermal radical polymerization technique. GO was used as the key additive to enhance the mechanical strength, fluid absorption capacity, coagulation stimulation and simultaneously to reduce wound adhesion force of CSAGs. It is hypothesized that CSAGs give full play to the advantages of hydrophilic materials for rapid hemostasis, and prevent secondary bleeding *via* anti-adhesive to the wound. To verify the hypothesis, the hemostatic performances of CSAGs were evaluated *via* rat femoral artery lethal hemorrhage model and rat liver lethal hemorrhage model, two commercial hemostats QuikClot® and CELOX™ were used as controls. Furthermore, the anti-adhesive properties of CSAGs were evaluated *via* rat dorsal adhesion model using QuikClot® gauze as a control. Finally, the anti-adhesion mechanism of CSAGs was fully investigated through the adhesion strength and peeling process of CSAGs from the tissue/scabs.

2. Materials and methods

2.1. Materials

Chitosan (molecular weight is 100–200 kg/mol, viscosity is 5–20 mPa.s, degree of deacetylation is 75–85 %) was obtained from Tokyo Chemical Industry (TCI). CELOX™ was obtained from Medtrade Products Ltd. (Crewe, U.K.). QuikClot® combat gauze was obtained from *Z*-Medica. SurgiSeal® was obtained from Adhezion BIOMEDICAL®. Graphite powders (80 mesh) were purchased from Qingdao Jinrilai Co., Ltd., Shangdong, China. Sodium nitrate ($NaNO_3$, AR), sulfuric acid (H_2SO_4, 98 %), hydrochloric acid (HCl, 37 %), ammonium persulfate (APS, 98 %), hydrogen peroxide (H_2O_2, 30 %), *N*,*N*′-Methylenebisacrylamide (MBA, 98 %) and potassium permanganate ($KMnO_4$, 99.9 %) were obtained from Sigma-Aldrich Co., Ltd. The graphene oxide (GO) solution was synthesized by using the modified Hummers' method (Hummers Jr & Offeman, 1958), and the concentration of GO solution was 10 mg/mL. Methacrylic anhydride was purchased from Bide Pharmatech Co., Ltd., Shanghai, China. Other reagents were obtained from Sinopharm Chemical Reagent Co., Ltd., and used as received unless otherwise stated.

2.2. Synthesis of methacrylamide chitosan (MAC)

The synthetic route of MAC was shown in Fig. S1. Briefly, chitosan (1.2 g) was dissolved in 2 wt% acetic acid at room temperature (RT) with a magnetic stirrer for 12 h and then filtered to remove insoluble impurities to give a 3 wt% chitosan solution. Methacrylic anhydride was added to the chitosan solution at 1 M equivalents per chitosan repeat unit. The mixture was allowed to be reacted for 12 h at RT with constant shaking. The resulting milky suspension was dialyzed against (molecular weight cut-off range 8000–14,000) water for 3 days to remove by-product acrylic acid and unreacted methacrylic anhydride. The resultant MAC was obtained by freeze-drying for 5 days and stored at −20 °C until use. The chemical structure of MAC was determined by ^{1}H, ^{13}C, HSQC and HMBC NMR spectra (Fig. S2-S5). The degree of substitution of methacryloyl group on MAC was 28 %.

^{1}H NMR (600 MHz, D_2O): δ 5.65 (d, 2H, H-8, H-8′), 4.50 (s, 1H, H-1), 4.10–3.20 (m, 7H, H-2, H-2′, H-3, H-4, H-5, H-6), 2.73 (s, 1H, H-2″), 2.06 (s, 3H, H-9), 1.96 (s, 3H, H-7).

^{13}C NMR (600 MHz, D_2O): δ 18.0 (C-10), 22.4 (C-12), 55.5 (C-2, C-2′), 56.7 (C-2″), 60.3 (C-6), 72.2 (C-3, C-3′), 74.1 (C-3″), 74.9 (C-5, 5′, 5″), 78.1 (C-4, C-4′), 79.4 (C-4″), 101.5 (C-1, C-1′), 102.4 (C-1″), 122.0 (C-9), 139.1 (C-8), 172.5 (C-7), 174.8 (C-11).

2.3. Synthesis of CSAGs

CSAG composite sponges were prepared by MAC, acrylamide (AAM), and GO with APS as the initiator agent and MBA as a crosslinking agent. Hydrothermal synthesis and freeze-drying methods were adopted to fabricate the porous composite sponge. The procedures of CSAGs in detail were available in SI Materials and methods. The sponges were coded as $CSAG_0$, $CSAG_{10}$, $CSAG_{20}$, and $CSAG_{33}$, where the numbers after CSAGs represent the proportion (wt%) of GO, respectively. The sponge components in detail were shown in Table S1.

2.4. Characterization

Scanning electron microscopy (SEM, 7800) was employed to observe the inside structure of the CSAGs. Fourier transform infrared (FT-IR) spectra of the pure GO, the MAC, and the CSAGs were recorded over a

wave number range of 4000–500 cm^{-1}. Energy-dispersive spectrometry (EDS, Hitachi S-4700) was used to analyze the surface element content of the CSAGs.

Zeta potential (Malvern NanoSizer ZS 2000) was used to analyze the effect of GO addition on CSAGs potential, which helped to explore the contribution of charge to hemostasis. In brief, CSAGs were ground into powder and dissolved in water at 1 mg/mL, the suspension was fully dispersed by ultrasound for 3 h. The dispersion was directly tested for Zeta potential.

2.5. Liquid absorption performance

2.5.1. Porosity

The porosity of the sponge was determined according to reported methods (Yang et al., 2019). In brief, the sponge was cut into small pieces and immersed in ethanol for 30 min to allow the sponge to fully absorb ethanol. Then, the sponge was removed from ethanol and weighed immediately. Porosity was calculated by the following Eq: porosity (%) = $(W_2 - W_1)/(\rho V_0) \times 100$ %, where ρ represented the density of ethanol (0.785 g/cm^3), W_1 and W_2 represented the mass of the sponge before and after absorbing ethanol, V_0 represented the volume of sponge.

2.5.2. Liquid absorption rate and weight

The liquid absorption of CSAGs was evaluated by measuring the absorption rate of a drop of water and the amount of water absorbed. The process of water droplet absorption was observed by a high-speed camera at 40 frames per second, and the absorption rate was determined by calculating the number of frames required for the water droplet to completely absorb from the contacting sponge surface. Liquid absorption volume was determined by soaking the sponge in deionized water (DIW), and calculated by the following Eq: Abs. weight = $(W_2 - W_1)/V_0$, where W_1 and W_2 respectively represented the weight before and after CSAGs absorb water, V_0 represented the volume of the sponge.

2.6. Shape memory ability

The shape-memory property of the $CSAG_0$ and $CSAG_{33}$ were evaluated. The $CSAG_0$ and $CSAG_{33}$ were compressed with 70 % strain and achieved shape fixation. Shape memory was tested by contacting the shape-fixed $CSAG_0$ and $CSAG_{33}$ with water or blood or by compressing the water or blood out of the sponge. The process was recorded by a digital camera, shape recovery ratio and time were measured.

2.7. In vitro coagulation properties

2.7.1. Whole blood clotting index (BCI)

Fresh citrated whole blood (CWB) (blood: 3.8 % sodium citrate = 9:1) was obtained by mixing SD rat heart blood with sodium citrate. The sponge was cut into small pieces ($1 \times 1 \times 1$ cm^3) and incubated at 37 °C for 5 min. 110 μL recalcified CWB solution (100 μL CWB and 10 μL 0.2 M calcium chloride solution) was dropped onto the sponge surface and incubated at 37 °C for 5 min. 25 mL DIW was added to dissolve uncoagulated red blood cells. The absorbance of the obtained solution was measured at the wavelength of 542 nm (MAPADA UV-1100 spectrophotometer). 25 mL DIW and 110 μL CWB were utilized as the negative control. The BCI value is calculated by the following Eq: BCI (%) = $Abs_{sample}/Abs_{reference\ value} \times 100$ %, where Abs_{sample} and $Abs_{reference\ value}$ represented the absorbance values of the sample and the reference value, respectively.

2.7.2. APTT and PT assays

The prothrombin time (PT) and activated partial thromboplastin time (APTT) were tested with XL-1000e automatic coagulation analyzer (ZONCI, China). In brief, fresh CWB was centrifuged at 3000 rpm at 4 °C for 15 min to collect the supernatant to obtain platelet poor plasma (PPP). Sponge powder and PPP were mixed to obtain 1 mg /mL solution, PPP solution was utilized as the control group. The solution to be tested was incubated at 37 °C for 5 min and then put into the detection hole of an automatic coagulation instrument for detection.

2.8. Interaction with blood cells

2.8.1. Red blood cells (RBCs) and platelet adhesion assays

The interactions between the CSAGs and RBCs were investigated with the previously reported method with some modifications (Liang et al., 2019). Before the test, red blood cells suspension (RBCs) were prepared by centrifuging CWB at 3000 rpm for 15 min. 100 μL RBCs were dropped onto the top of the sponge (5 mg pieces) and incubated at 37 °C for 1 h. Then gently rinse the sponge with PBS to remove unadhered red blood cells, and 4 mL DIW was added to lyse RBCs and release hemoglobin for 1 h. The OD value of supernatant was measured at 540 nm, and 100 μL RBCs and 4 mL DIW were utilized as the control group. The percentage of adherent erythrocytes is calculated by the following Eq: RBCs adhesion (%) = $OD_{sample}/OD_{reference\ value} \times 100$ %, where OD_{sample} represented the OD value of sponge at 540 nm, and $OD_{reference\ value}$ represented the OD value of the control group at 540 nm.

The interactions between various hemostats and platelets were further evaluated. Before the test, the platelet-rich plasma (PRP) was prepared by centrifuging CWB at 1500 rpm for 5 min. 50 μL PRP were dropped onto the top of the sponge (5 mg pieces) and incubated at 37 °C for 1 h. Then gently rinse the sponge with PBS to remove unadhered platelets, 0.6 mL of 1 % Triton X-100 was used to lyse attached platelets for 1 h at 37 °C to release lactate dehydrogenase (LDH) enzyme. The LDH content was determined by Determined by LDH kit (Biyuntian, China). 50 μL PRP were utilized as the control group, and the OD value of the solution at 490 nm was determined. The percentage of adherent platelets was calculated by the following Eq: platelets adhesion (%) = $OD_{sample}/OD_{reference\ value} \times 100$ %.

2.8.2. Platelet activation test

In brief, sponges ($1 \times 1 \times 0.25$ cm^3 pieces) were immersed in PBS and incubated at 37 °C for 2 h. PRP was added to PBS at a volume ratio of 1:20, and the mixture was incubated at 37 °C for 1 h. Soaked sponge were dehydrated with 50 %, 60 %, 70 %, 80 %, 90 %, and 100 % ethanol, each for 10 min. Freeze-drying and metal-spraying processes were finished for SEM observation.

2.9. In vivo hemostatic properties

Rat liver perforation wound model was used to assess the hemostatic properties of CSAGs for deep incompressible wounds. All animals were treated and cared for in accordance with the National Research Council's Guide for the care and use of laboratory animals and under supervision and assessment by the SPF Animal Department of Clinical Institute in China−Japan Friendship Hospital (Approval no. 211001).

SD rats (250–280 g, 8 weeks) were anesthetized by intraperitoneal injection of 10 % chloral hydrate (1 mL per 200 g rat weight). The thoracic cavity was opened with surgical scissors, and circular perforations were made in the liver using a punch (7 mm in diameter). Then the liver was placed on pre-weighed double-layer filter paper, and the pre-compressed sponge (12 mm before compression, 6 mm after compression) was immediately filled into the liver hole to stop bleeding. Blood loss and time to hemostasis were recorded. The SD rats were euthanized by cervical dislocation.

A femoral artery injury model was used to assess the hemostatic properties of the $CSAG_{33}$ for severe, large wounds. SD rats (250–280 g, 8 weeks) were anesthetized, the epithelial tissue and muscle were cut with a scalpel to fully expose the rat's femoral artery. The vessel was completely cut off with a scalpel to create uncontrolled hemorrhage, and materials were applied to the arterial wound area with appropriate pressure. After the hemostasis was completed, the weight of the material

after hemostasis was subtracted from the weight of the material before hemostasis to obtain the blood loss, and the hemostasis time was recorded.

2.10. In vivo anti-adhesion properties

The anti-adhesion properties of the sponge on the wound were evaluated by using the rat back adhesion model. The rat back adhesion test was adapted from previous reports (Li et al., 2019). The back hair of anesthetized rats (250–280 g, 8 weeks of age) was removed with a shaver and depilated with Veet depilatory cream, and the back skin was disinfected with 75 % *v*/v ethanol. Use the scalpel to make two incisions with a length of 1 cm on the back of the rat. Materials ($1 \times 1.5 \times 0.2$ cm^3) were applied to the wound and gently pressed to ensure that the wound fits with the sponge for 1 h, so as to make the blood clot fully mature and coagulate. We only gently compressed the dressing to ensure good contact between the wound and the dressing. Then we fixed the sponge with the lower hem of the tension machine and peel the sponge vertically along the wound to measure the maximum peeling force of the sponge in the process of peeling from the wound.

2.11. Adhesion between CSAGs and tissue/scab

The inner surface of porcine skin and fat-removing porcine intestine were fixed to the petri dish, and sponges ($CSAG_0$, $CSAG_{10}$, $CSAG_{20}$, $CSAG_{33}$) were placed on a fixed mucosal surface and a pressure of 100 g was applied for 1 min. Finally, sponges were gently removed and porcine skin and mucosal surface state were recorded by a digital camera.

Adhesive properties of tissue and scab were determined according to previously reported methods with a slight modification (Li et al., 2018a, b). A surface tensiometer (DCAT 21) was used to measure adhesion strength. Preparation of clot: Recalcified CWB and frozen fresh plasma (FFP) (100 μL CWB/FFP and 10 μL 0.2 M calcium chloride solution) was added dropwise to the plate, and the blood coagulated for 30 min at room temperature and suitable humidity to form a blood scab. Sponges ($0.5 \times 0.5 \times 0.5$ cm^3 pieces) were fixed on the machine with a thin line, and tissue/scab was fixed on the lifting table. Sponges were attached to the surface of tissue/scab and pressurized with a weight of 20 g for 1 min to make it fully bonded. With the operation of the tensiometer, the sponge was gradually separated from the tissue/scab surface, and the mass distance curve of adhesion strength was obtained.

2.12. Peeling CSAGs from material/scab composite

A 2×8 mm^2 rectangular hole was cut out of the side wall of the silicone tube, the fresh porcine skin was fixed on the periphery of the tube and a hole was cut out at the same position; the lower end of the tube was sealed, and blood was added from above to simulate real vascular bleeding. Calcified anticoagulant whole blood (1 mL) was dripped between the pig skin and the material for 1–2 h to form blood scabs to seal the wound. Then blood was injected into the tube, and the material was gently stripped from the wound to observe whether the wound is bleeding.

2.13. In vitro hemolysis

The hemolysis test was adapted from previous reports with some changes (Li et al., 2016). Sponge powder was added to PBS and treated with ultrasound for 2 h to prepare the concentration of 15.6, 31.3, 62.5, 125, 250, 500 and 1000 μg/mL dispersion. 0.2 mL of diluted RBCs were added into 0.8 mL dispersions of different concentrations. All samples were incubated at 37 °C for 3 h, and then centrifuged at 10000 *g* for 5 min. The OD value of obtained supernatant was read at 540 nm, PBS (+RBCs) and deionized water (+RBCs) were utilized as negative and positive controls. The hemolysis rate was calculated by the following Eq: hemolysis (%) $= (OD_{sample} - OD_{negative})/(OD_{positive} - OD_{negative}) \times 100$ %, where Abs_{sample}, $Abs_{negative}$ and $Abs_{positive}$ are the absorbance values of the sample group, the negative group and the positive group at 540 nm, respectively.

2.14. Cytotoxicity evaluation

The cytotoxicity of sponge on mouse fibroblast L929 (from cell resource center, IBMS, cams/PUMC, Beijing, China) was evaluated by the leaching method. Firstly, the sponge was cut into 5 mg pieces and mixed with RPMI-1640 medium at the concentration of 10 mg/mL at 37 °C for 24 h to obtain the leaching solution. The complete medium (CM) was composed of 90 % RPMI-1640 medium, 10 % fetal bovine serum (FBS) and 1 % antibiotics. The L929 cells will be regulated to 5×10^4/mL in CM and cultured at 37 °C (5 % CO_2) for 12 h. The medium was replaced with the leaching solution for 24 h, and CM containing unreacted RPMI-1640 medium was used as the control group. After PBS washing the cells two to three times, 5 mg/mL 3-(4,5-dimethylthiazol-2-yl)-2,5-diphenyltetrazole bromide (MTT) solution was added and culture at 37 °C for another 4 h. The OD value at 490 nm of the supernatant was read, and the cell viability RGR was calculated by the following Eq: RGR (%) $= OD_{test}/OD_{reference\ value} \times 100$ %, where OD_{test} is the absorbance of sponge group at 490 nm, $OD_{reference\ value}$ is the absorbance of the control group at 490 nm.

2.15. Statistical

All tests were processed in triplicate and similar results were acquired. GraphPad Prism 8 software was used for statistical analysis of the data. Values are expressed as the means ± standard deviation (SD). Student's *t*-test was used for the treatment comparison. *P*-values <0.05 were considered to be statistically significant difference.

3. Results and discussion

3.1. Synthesis and characterization of CSAGs

The MAC/GO composite sponges, CSAGs, were constructed *via* the free radical polymerization technique. MAC and AAM formed a cross-linked network through olefin polymerization in the presence of the initiator APS; at the same time, GO covalently bonded on the network by ring-open reaction of epoxy (Fig. 1a). To study the effects of different GO addition on the physicochemical properties of the sponges, a series of CSAGs ($CSAG_0$, $CSAG_{10}$, $CSAG_{20}$, $CSAG_{33}$) were prepared by varying GO proportions (0, 10, 20, 33 wt%) (Table S1). While GO proportion was >33 wt%, the construction of CSAG was failed. Thus, the CSAGs added >33 wt% of GO would not be discussed in the follow-up.

The CSAGs colors changed from white to brown with the increased addition of GO (Fig. 1b). $CSAG_0$ (without GO) exhibited a compact packing structure. Differently, $CSAG_{10}$, $CSAG_{20}$, and $CSAG_{33}$ possessed a porous structure, and their pore size gradually increased (Fig. 1c). The porosity of CSAGs increased from 31.3 % for $CSAG_0$ to 79.3 % for $CSAG_{33}$ ($^{####}$, $p = 0.000009$, Fig. 1d). This implied that adding GO sheets quenched partial free radicals in polymerization, resulting in a loose cross-linking network (Wenjing et al., 2022; Yan et al., 2018) (Fig. S6 and S7). Therefore, $CSAG_{33}$ showed high porosity. The successful construction of CSAGs by addition reaction and curing reaction was further demonstrated by FTIR spectra and elemental analysis. The absorption signal of C═C stretching vibration (1546 cm^{-1}) belonging to MAC disappeared (Xie et al., 2020), as well as the epoxy stretching peak strength (860 cm^{-1}) belonging to GO decreased (Acik et al., 2011) (Fig. 1e). The C/N of $CSAG_0$, $CSAG_{10}$, $CSAG_{20}$, and $CSAG_{33}$ sponge gradually increased with the GO addition, 3.7, 4.1, 4.8 and 5.4, respectively (Fig. 1f). Additionally, their zeta potential also decreased gradually and tended towards electrical neutrality (Fig. 1g) because of the shielding effect of negatively charged GO.

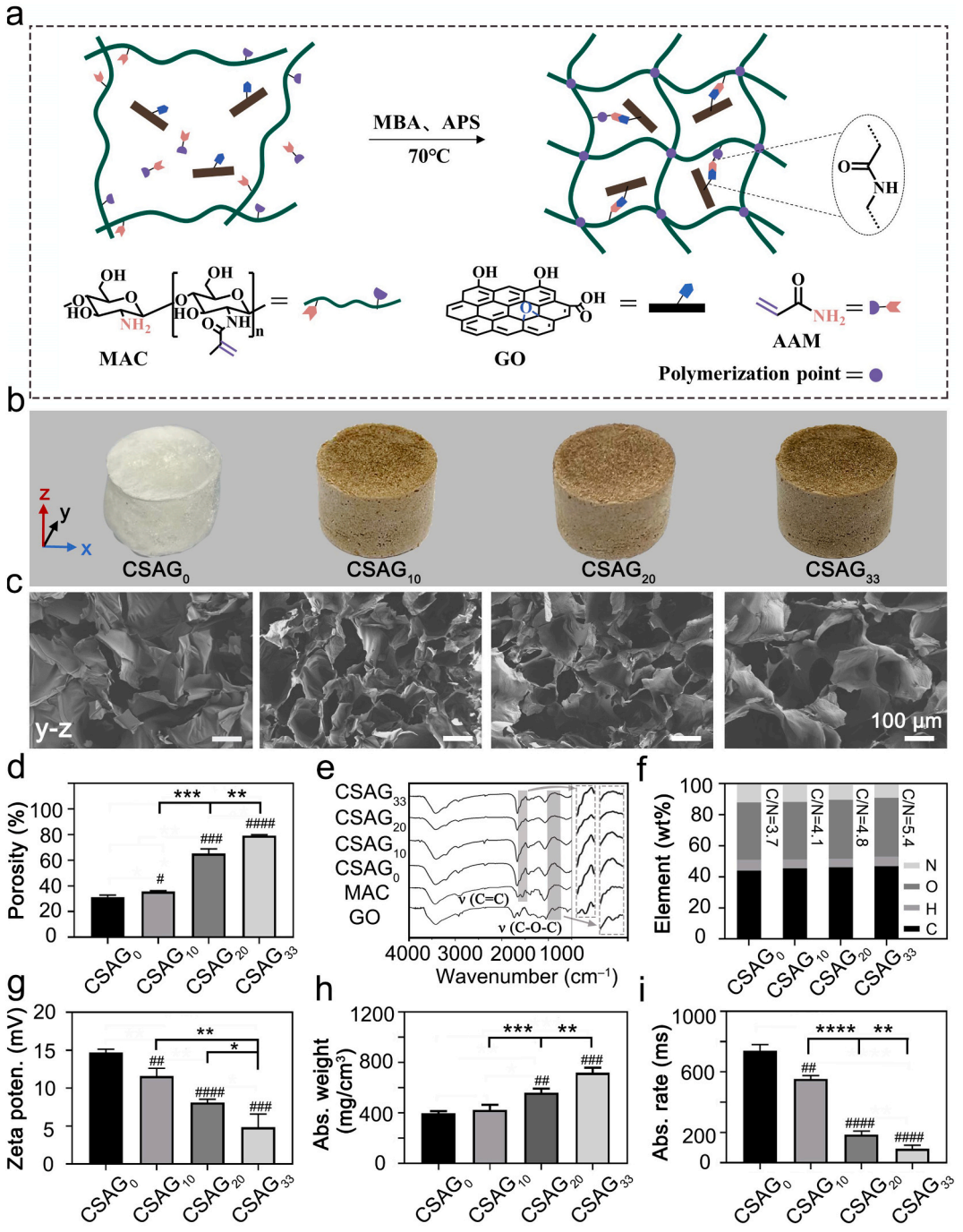

Fig. 1. Characterization of CSAGs. (a) Preparation process of CSAGs; (b) Photograph and (c) cross section SEM image of the $CSAG_S$; (d) Porosity of CSAGs; (e) FT-IR spectra of CSAGs, MAC and GO; (f) Elemental analysis of CSAGs; (g) Zeta potential, (h) water absorption and (i) absorption rate of a drop of water of $CSAG_S$. Error bar indicate S·D ($n = 3$), # means the contrasts between experimental groups and $CSAG_0$, $^{\#/*}p < 0.05$, $^{\#\#/**}p < 0.01$, $^{\#\#\#/***}p < 0.001$, $^{\#\#\#\#/****}p < 0.0001$.

GO doping could notably improve the absorption characteristics of CSAGs. Their liquid absorption capacity was correlated positively with the content of GO, which increased significantly from 397 mg/cm^3 of $CSAG_0$ to 718 mg/cm^3 of $CSAG_{33}$ ($^{\#\#\#}$, $p = 0.0002$, Fig. 1h). Furthermore, by altering their wettability and providing water transport channels, GO could accelerate the liquid absorption rate of CSAGs (Depan et al., 2011; Hegab & Zou, 2015; Zhang et al., 2021a, b). The liquid absorption rate of CSAGs decreased from 740 ms for $CSAG_0$ to 93 ms for $CSAG_{33}$ ($^{\#\#\#\#}$, $p = 0.00002$, Fig. 1i, Fig. S8). Therefore, $CSAG_{33}$ has a high absorption capacity and ultrafast liquid absorption rate, both of which were critical for hemostatic materials when dealing with severe trauma bleeding.

3.2. Shape memory characteristics

Accordingly, the shape memory property of $CSAG_{33}$ was then studied. As shown in Fig. 2a, $CSAG_{33}$ was easily fixed and rapidly restored its original shape after liquid (water/blood) absorption by filling liquid into the porous cavity through the rapid absorption characteristic. It recovered to >93 % compression height in water or blood ($^{\#\#\#\#}$, $p = 0.000002$) within 3 s ($^{\#\#\#\#}$, $p = 0.00032$, Fig. 2b, c). In contrast, $CSAG_0$ only recovered to 14 % in water and did not even rebound in blood. This implied that GO additives played pivotal parts in strengthening the durability and mechanical integrity of CSAGs. The interconnected porous structures in $CSAG_{33}$ could withstand compression by

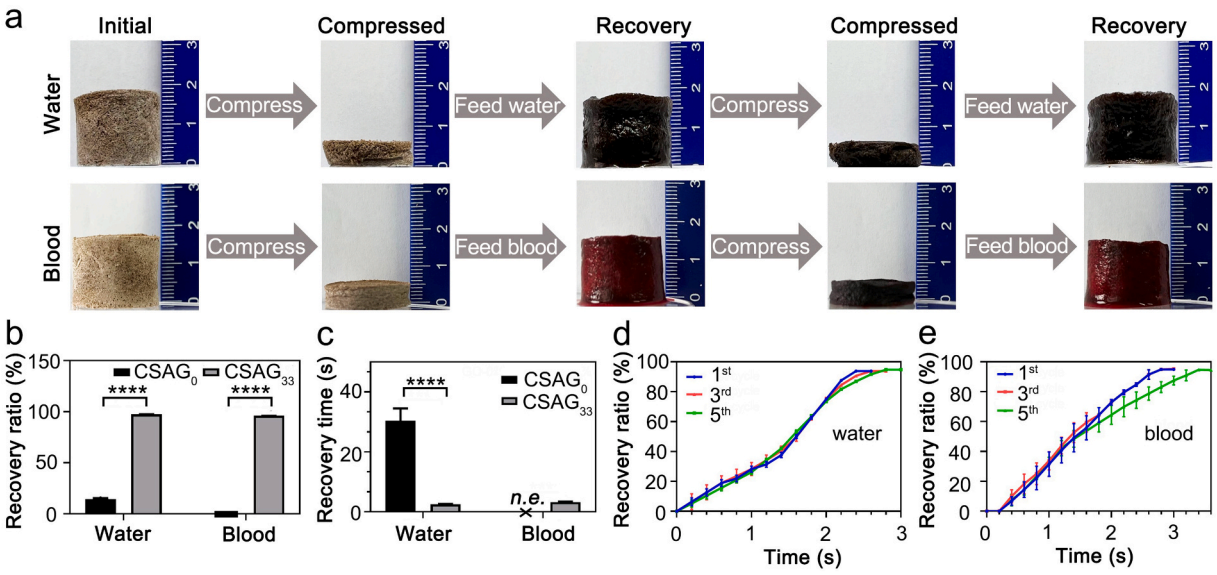

Fig. 2. Mechanical properties of CSAGs. (a) Photographs shape memory performance of $CSAG_{33}$ in water and blood. (b) Recovery ratio and (c) recovery time of $CSAG_0$ and $CSAG_{33}$ in water and blood. The recovery ratio of $CSAG_{33}$ rebound in (d) water or (e) blood at 1, 3, 5 compression-recovery cycles. Error bar indicate S·D ($n = 3$), ****p < 0.0001.

transferring the mechanical stress (Li et al., 2020b, b). In the cyclic compression rebound test (Fig. 2d, e), $CSAG_{33}$ maintained a high rebound ratio (93 %) and short rebound time (2.6 s) after five cycles of compression in water. In terms of blood, it only showed a slight extension of rebound time (0.6 s) at the fifth cycle of compression. Overall, $CSAG_{33}$ sponge has fast and stable shape memory characteristics that aid the hemostasis of deep incompressible wounds.

3.3. Blood cells and platelets adhesion properties

The first stage of coagulation process is the aggregation and activation of red blood cells and platelets, and the subsequent formation of the initial clotting plug. As such, we quantitated the blood cell aggregation ability of CSAGs. The commercial hemostats, QuikClot® combat gauze and CELOX™ powders were used as controls. As shown in **Fig. 3a** and **b**, the adsorption ratio of red blood cells and platelets in $CSAG_0$ group were 40.9 % and 50.9 %, respectively, which were significantly higher than those in QuikClot® (6.8 %, ****, $p = 0.000033$; and 6.2 %, ***, $p = 0.000682$) and CELOX™ groups (10.1 %, ****, $p = 0.000005$; and 12.2 %, ****, $p = 0.000019$). Notably, CELOX™ is also positively charged, but its capacity for red blood cells adsorption is far less than that of $CSAG_0$. Interestingly, the adsorption of red blood cells and platelets by $CSAG_{33}$ was 8.3 % (*, $p = 0.0116$) and 4.4 % (*, $p = 0.0307$) higher than those of $CSAG_0$, respectively. This indicated that negatively charged GO addition might not attenuate the blood-cells capture ability of chitosan-based sponge. Importantly, the increasing porosity of $CSAG_{33}$ provided a

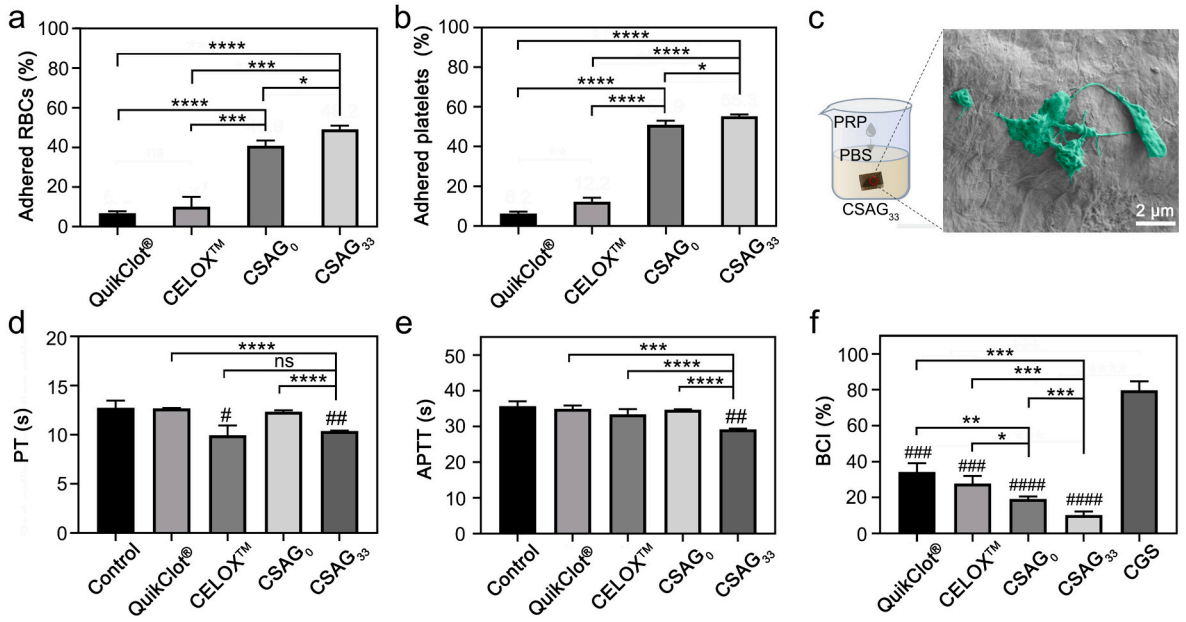

Fig. 3. *In vitro* clotting properties of CSAGs. (a) RBCs and (b platelets adsorption ratio of QuikClot®, CELOX™, $CSAG_0$ and $CSAG_{33}$. (c) SEM images of interfacial interaction between platelets and the $CSAG_{33}$. (d) PT, (e) APTT and (f) BCI test of $CSAG_0$, $CSAG_{33}$, QuikClot®, CELOX™ and cross-linked graphene sponge (CGS). Error bar indicate S·D (n = 3), # means the contrasts between experimental groups and control, $^{\#/*}p < 0.05$, $^{\#\#/**}p < 0.01$, $^{\#\#\#/***}p < 0.001$, $^{\#\#\#\#/****}p < 0.0001$.

large number of absorption channels, significantly facilitating the capture and storage ability of red blood cells and platelets. To elucidate the effect of CSAGs on platelet activation, $CSAG_{33}$ was immersed in a PBS solution containing PRP (Fig. 3c). Free platelets in PBS were adsorbed on the surface of $CSAG_{33}$ and displayed pseudopodia-like morphology, indicating platelets activation on the surface of $CSAG_{33}$. These results demonstrated that $CSAG_{33}$ could effectively accumulate blood cells and activate platelets, which was in favor of accelerating the formation of primary clotting plugs.

3.4. *In vitro coagulation properties*

The second stage of coagulation process is the reinforcement of the initial clotting plug by activating the cascade response of coagulation. Accordingly, the coagulation indexes, PT and APTT, were used to assess the activation of endogenous and exogenous coagulation pathways by CSAGs. The PT of $CSAG_{33}$ decresed notably from 12.7 s to 10.4 s ($^{\#\#}$, $p = 0.0052$), and showed no significantly difference with that of CELOX™ (9.9 s, ^{ns}, $p = 0.498$, Fig. 3d). $CSAG_0$, on the other hand, did not show exogenous coagulation stimulation accompanied with an unchanged PT value. These results demonstrated that the presence of GO was required

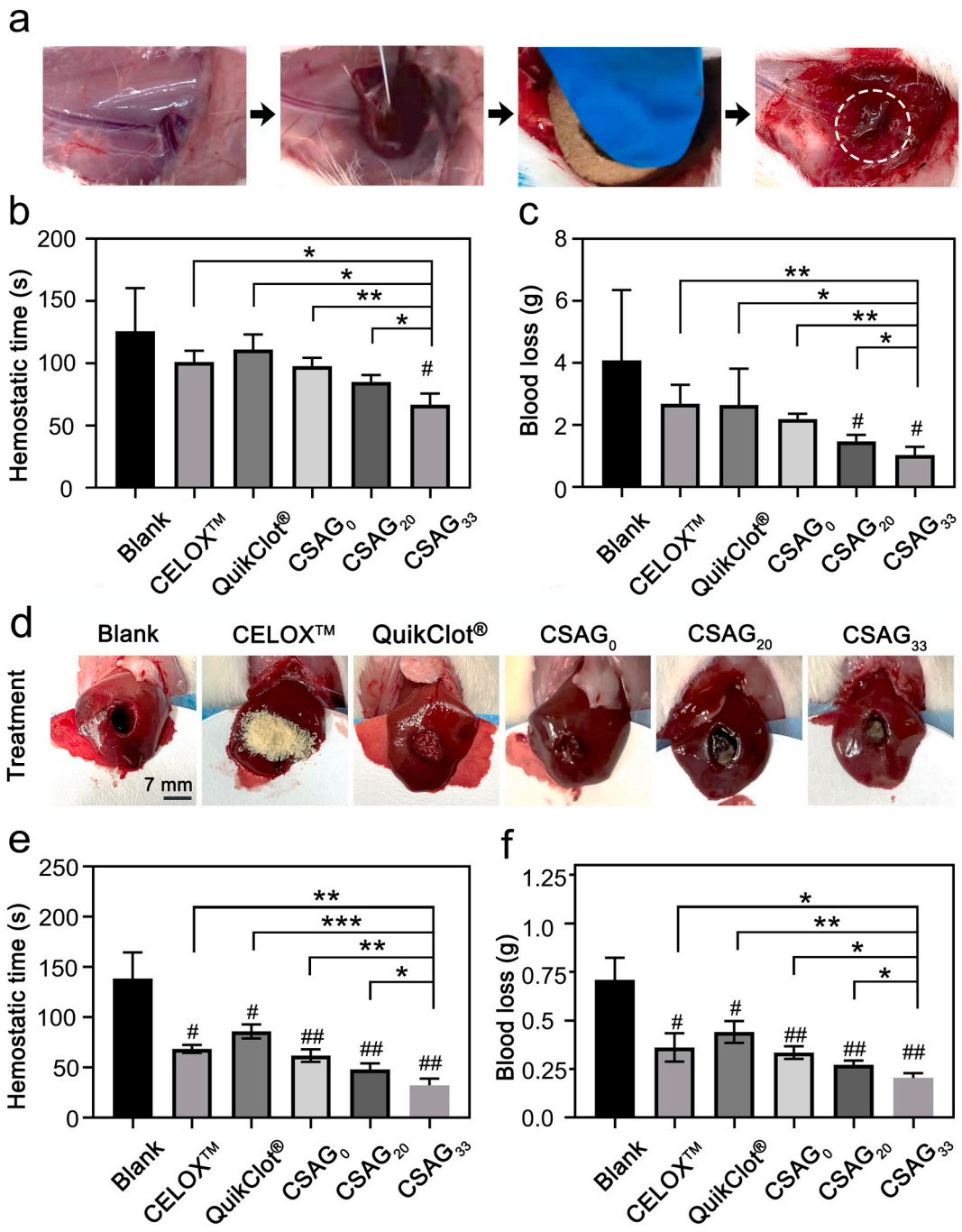

Fig. 4. *In vivo* hemostasis and anti-adhesion performance of CSAGs. (a) Hemostatic process of $CSAG_{33}$ in SD rat artery injury model. (b) Hemostatic time and (c) blood loss of blank, CELOX™, QuikClot®, $CSAG_0$, $CSAG_{20}$ and $CSAG_{33}$ in SD rat artery injury model. (d) Hemostasis of the materials in SD rat liver punching model. (e) Statistical hemostatic time and (f) blood loss of blank, CELOX™, QuikClot®, $CSAG_0$, $CSAG_{20}$ and $CSAG_{33}$ in SD rat liver punching model. Error bar indicate S·D ($n = 5$), # means the contrasts between experimental groups and blank, $^{\#/*}p < 0.05$, $^{\#\#/**}p < 0.01$, $^{\#\#\#/***}p < 0.001$.

for $CSAG_{33}$ to excite exogenous coagulation stimulation. Similarly, $CSAG_{33}$ also stimulated the endogenous coagulation pathway, significantly decreasing the APTT value from 35.7 s to 29.2 s ($^{\#\#}$, $p = 0.0011$, Fig. 3e). This could be attributed to the negatively charged carboxyl functional group of GO, which could activate the transformation of coagulation factor XII to XIIa. As such, $CSAG_{33}$ would promote blood clotting by simultaneously activating exogenous and endogenous coagulation pathways. Accordingly, the BCI of $CSAG_{33}$ was then used to evaluate their final blood clotting ability *in vitro* (Fig. 3f). The lower BCI value showed the lower heme content released by the blood, representing the better blood coagulation performance. The BCI values of CSAGs were significantly lower than CGS (79.7 %), indicating that CSAGs have excellent *in vitro* coagulation properties. $CSAG_0$ (19.2 %) showed lower BCI values than the commercial hemostat, QuikClot® (34.2 %; **, $p = 0.0068$) and CELOX™ (27.7 %; *, $p = 0.0316$), suggesting that micro-pore structure was benefited for blood clotting. Moreover, GO addition could accelerate liquid absorbability and trigger coagulation stimulations of CSAGs, thereby reinforcing hemostatic performance. The $CSAG_{33}$, therefore, exhibited the lowest BCI values (10.2 %; $^{\#\#\#\#}$, $p = 0.00002$) among all the experimental groups. These results indicated that $CSAG_{33}$ possessed excellent hemostatic efficiency *in vitro*.

3.5. In vivo hemostasis of CSAGs

The assays of hemolysis and cell tocxicity were first conducted and revealed the high biocompatibility of $CSAG_{33}$ (Fig. S9 and S10). Subsequently, the bleeding control and anti-adhesive properties of CSAGs were evaluated using a rat femoral artery injury model (Fig. 4a). In this case of severe bleeding, $CSAG_{33}$ was able to absorb blood quickly without overflowing, resulting in successful hemostasis. Statistical analysis revealed that CSAG33 exhibited the best hemostatic performance (Fig. 4b and c), it stopped the bleeding within 66.7 s ($^{\#}$, $p = 0.0410$), which was 34 %, 40 %, 18 % and 32 % faster than CELOX™, QuikClot®, $CSAG_{20}$ and $CSAG_0$, respectively. Hydrophilic materials like gauze, have been reported to absorb large amounts of blood, resulting in excessive blood loss. Differently, $CSAG_{33}$ possessed hydrophilic properties while minimized blood loss significantly. $CSAG_{33}$ had the lowest blood loss of 1.03 g ($^{\#}$, $p = 0.0340$), which was 62 %, 61 %, 23 % and 53 % less than CELOX™, QuikClot®, $CSAG_{20}$ and $CSAG_0$, respectively. These results were mainly due to the fact that hydrophilic $CSAG_{33}$ could rapidly absorbs plasma, enriches blood red blood cells and platelets at the bleeding site, and promotes the rapid formation of primary clotting clots. At the same time, $CSAG_{33}$ displayed multiple coagulation stimuli to promote rapid fibrin production. As a result, a stable blood scab forms quickly at the wound to stop the bleeding. In addition, $CSAG_{33}$ can be easily detached from the wound with a slight adhesion to the tissue (Fig. S11). After detachment, a dark red scab remained steadily in the wound that avoided secondary bleeding (the white circle in Fig. 4a). Therefore, $CSAG_{33}$ was effective in controlling severe bleeding and enabling safe debridement.

Subsequently, a rat liver injury model was further used to evaluate the hemostatic potential and anti-adhesion property of $CSAG_{33}$ for noncompressible wounds (Fig. 4d). Significantly, the hemostatic time of $CSAG_{33}$ was reduced to 32.3 s compared with 138.3 s of the untreated blank group ($^{\#\#}$, $p = 0.0025$, Fig. 4e). Furthermore, it was about 53 %, 62 %, 33 % and 48 % lower than those of CELOX™ (68.7 s, **, $p = 0.0013$), QuikClot® (86.0 s, ***, $p = 0.0007$), $CSAG_{20}$ (62.0 s, **, $p = 0.0049$) and $CSAG_0$ (48.0 s, *, p = 0.0410). The blood loss of $CSAG_{33}$ group decreased to 0.20 g from 0.71 g of the blank group ($^{\#\#}$, $p = 0.0026$), which was about 44 %, 54 %, 26 % and 41 % lower than those of CELOX™ (0.36 g, *, $p = 0.0482$), QuikClot® (0.44 g, **, p = 0.0026), $CSAG_{20}$ (0.27 g, *, $p = 0.0274$) and $CSAG_0$ (0.34 g, *, $p = 0.0336$; Fig. 4f). The results showed that the hemostatic performance of CSAGs were positively correlated with the GO addition amount. The excellent hemostatic properties of $CSAG_{33}$ are mainly accounted for its rapid shape recovery ability (Fig. 2). When $CSAG_{33}$ came into contact with blood, it quickly absorbed plasma and returned to its original shape, which filled the wound and applied sufficient pressure to stop bleeding. Conversely, CELOX™ and $CSAG_0$ could not expand to fill the wound nor quickly form blood scabs, resulting in continuous bleeding. Interestingly, the $CSAG_{33}$ sponge could be easily removed from the liver hole without causing wound tearing and secondary bleeding, and no sponge residue was found on the pore wall (Fig. S12). Therefore, $CSAG_{33}$ shows good hemostatic and anti-wound adhesion effects in deep noncompressible wounds.

3.6. In vivo rat back incision anti-adhesion of CSAGs

In order to further investigate the anti-adhesive properties of CSAGs, a classical rat dorsal incision model was used to quantitatively evaluate their peeling force. As shown in Fig. 5a, gentle pressure was applied to the materials (QuikClot®, $CSAG_0$ and $CSAG_{33}$) to fit the bleeding wound. After 2 h, the materials were slightly stripped from the wound (Fig. 5b-5d). It could be observed that QuikClot® and $CSAG_0$ adhered strongly to the tissue. The tissue was pulled up to >1 cm without peeling off the material (Fig. 5b′ and c′, Video S1). The wounds were severely torn after the material peeling, and secondary bleeding was observed (Fig. 5b″ and 5c″). On the contrary, $CSAG_{33}$ could be easily stripped from the wound (Fig. 5d′, Video S2), and the wound in $CSAG_{33}$ group was tightly closed without secondary bleeding (Fig. 5d″). Quantitatively, $CSAG_{33}$ showed the lowest wound peeling force of 213 mN, which was 79.3 % and 56.5 % lower than QuikClot® and $CSAG_0$ (1031 mN, *, $p = 0.0125$ and 490 mN, $^{\#}$, $p = 0.0298$, respectively, Fig. 5e). The medical wound sealant SurgiSeal® sealed the wound well, but its strong adhesive caused severe tearing of the wound and secondary bleeding during the peeling (Fig. S13, Video S3). Comparatively, the peeling strength of $CSAG_{33}$ was 86 % lower than that of SurgiSeal® (Fig. S14), which can effectively prevent secondary damage. In addition, The tissue-peeling force of $CSAG_{33}$ was about 10 times smaller than that of hydrocolloid dressings, and was about 5 times smaller than that of polyurethane and acrylate dressings (Klode et al., 2011). Therefore, $CSAG_{33}$ significantly weakened the adhesion to the tissue for easy, non-secondary damage peeling.

3.7. Exploring the anti-adhesion mechanism of CSAGs

Accordingly, anti-adhesion mechanisms of CSAGs were studied (Fig. 6a). The adhesion of materials and tissue were first investigated using porcine skin and intestinal mucosa. The CSAGs were found to be intact remained intact after being peeled from the inner surface of the porcine skin, and there were no material residue on the porcine skin (Fig. 6b). However, when porcine intestinal mucosa was used instead of the porcine skin, $CSAG_0$ and mucosa formed a strong adhesion, which resulted in material broken to numerous residues during the peeling process (Fig. 6b, Fig. S15). Differently, $CSAG_{10}$, $CSAG_{20}$ and $CSAG_{33}$ were easier to peel off than $CSAG_0$, and there are no material rupture or residues. These results could be attributed to the GO addition. It could improve the mechanical strength of CSAGs on the one hand; on the other hand, GO addition might attenuate the adhesion between CSAGs and tissue, thereby modulating the interfacial interaction (Hamedi, Moradi, Hudson, Tonelli, & King, 2022).

To verify the above conjecture, the peel strength of CSAGs against porcine mucosal tissue was quantified by a crack-opening model (Mati-Baouche et al., 2014) (Fig. 6c, Fig. S14). The adhesion force was a strictly negative correlation with the content of GO addition (Fig. 6d). The peel strength of $CSAG_0$, $CSAG_{10}$, $CSAG_{20}$ and $CSAG_{33}$ against the porcine tissue were 9.03 kPa, 8.56 kPa (^{ns}, $p = 0.2$), 6.41 kPa (***, $p = 0.0008$) and 4.78 kPa (*** $p = 0.0002$), respectively. This implied that GO obviously weakened the adhesion of CSAGs to tissue. Furtherly, the peel strength of CSAGs against blood scab was evaluated (Fig. 6e). The peel strength of $CSAG_0$ against blood scab was 0.24 kPa, and that of

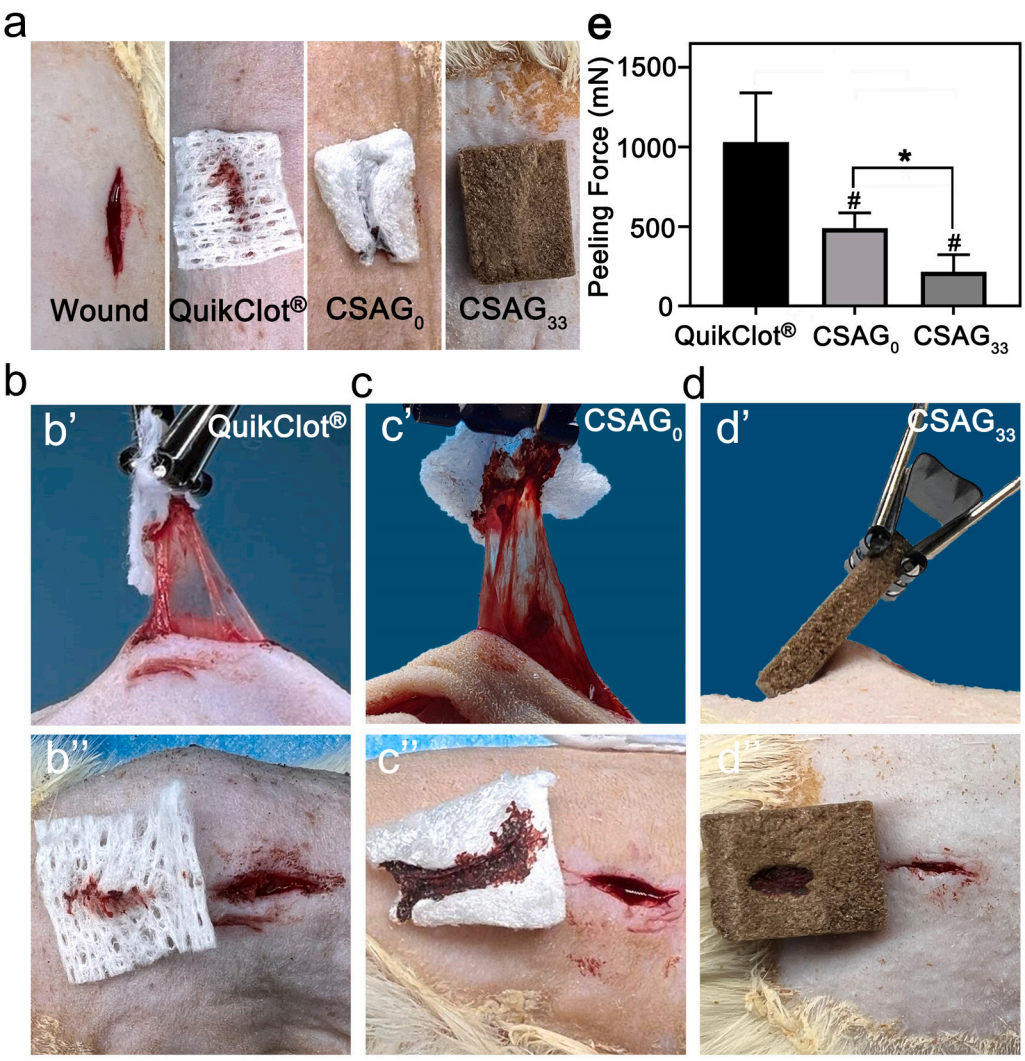

Fig. 5. *In vivo* anti-adhesion assays of CSAGs. (a) Photographs of wound in rat back incision adhesion model, QuikClot®, $CSAG_0$ and $CSAG_{33}$ applied on the wounds. Photographs of (b) QuikClot®, (c) $CSAG_0$ and (d) $CSAG_{33}$ peeling process (b′, c′ and d′ represent the material and wound state during peeling; b″, c″ and d″ represent the material and wound state after peeling). (e) Peeling force of QuikClot®, $CSAG_0$ and $CSAG_{33}$. Error bar indicate S·D ($n = 3$), # means the contrasts between experimental groups and QuikClot®, $^{\#/*}p < 0.05$.

$CSAG_{10}$ (0.18 kPa, ^{ns}, $p = 0.06$), $CSAG_{20}$ (0.15 kPa, **, $p = 0.003$) and $CSAG_{33}$ (0.12 kPa, **, $p = 0.002$) decreased gradually, which was consistent with the results of adhesion between CSAGs and tissue. $CSAG_{33}$ showed the lowest peel strength either against tissue and scab, fully confirming its outstanding *in vivo* anti-adhesion properties. Interestingly, the peel strength of $CSAG_{33}$ against blood scab was one order of magnitude lower than that against tissue (Fig. 6f). The difference in peeling strength may be due to the different composition of the two. i) The tissue surface has various proteins, glycogenic substances, *etc.*, which provide abundant functional groups to interact with CSAGs (hydrogen bonding, electrostatic forces, *etc.*) (Hamedi et al., 2022; Mati-Baouche et al., 2014). ii) Comparatively, the whole blood clot is composed of fibrin, platelets and red blood cells (RBCs). The surface of the clot is mainly fibrin which containing fewer types and quantities of functional groups than tissue, leading to weak interaction (Ariëns, 2016; Mosesson, 2005). Besides, during the clot contraction, fibrin forms a dense and hydrophobic network structure, which lead to further weakening of CSAG adhesion to the clot (Cines et al., 2014; Hamedi et al., 2022; Wang et al., 2022; Weisel & Litvinov, 2017). We also investigated the effect of RBCs on adhesion. The peeling strength of $CSAG_0$, $CSAG_{10}$, $CSAG_{20}$ and $CSAG_{33}$ against the FFP clots were 1.83 kPa, 1.51 kPa, 1.03 kPa and 0.80 kPa, respectively. Interestingly, the peeling strength of FFP clots was slightly higher than that of CWB clots (Fig. S16). This may be because the absent RBCs decreased the mechanical strength of the clot, which resulted in a larger contact area with the CSAGs when compression, and thus increased the adhesion strength compared to CWB clots (Liang, Chernysh, Purohit, & Weisel, 2017). Nevertheless, the adhesion strength of the FFP clot was much less than that of the tissue. Therefore, it was concluded that the composition leads to the difference in adhesion strength between tissue and blood clot, which is consistent with our previous conclusions. Anyway, this result demonstrated that the adhesion between the materials and tissue, rather than adhesion between the materials and blood scab, led to severe laceration and secondary bleeding.

Additionally, the formed material/scab composite was a problem that could not be ignored. A prevailing view is that a superhydrophobic surface prevents secondary bleeding by avoiding the formation of material/scab composites; but traditional hydrophilic hemostatic materials, *e.g.* gauze, will absorb a large amount of blood and sequentially form the composite, which may lead to the rupture of scab and secondary bleeding (Wang et al., 2019; Zhang et al., 2013). Accordingly, we studied the peeling process of $CSAG_{33}$ from the material/scab composite (Fig. 7a). It could be observed that the blood unimpeded flew out from the 'wound' once injected into the silicone tube (Fig. 7b, Video S4); while the wound was blocked by the $CSAG_{33}$/scab composite, the blood was stably enclosed in the tube (Fig. 7c). Then, the $CSAG_{33}$ was slightly peeled off from the wound (Video S5). Interestingly, the $CSAG_{33}$/scab composite could be ripped along the interface. The residue scabs on tissue retained a certain thickness, effectively preventing the blood from flowing out of the tube (Fig. 7d). The surfaces of the separated scab were

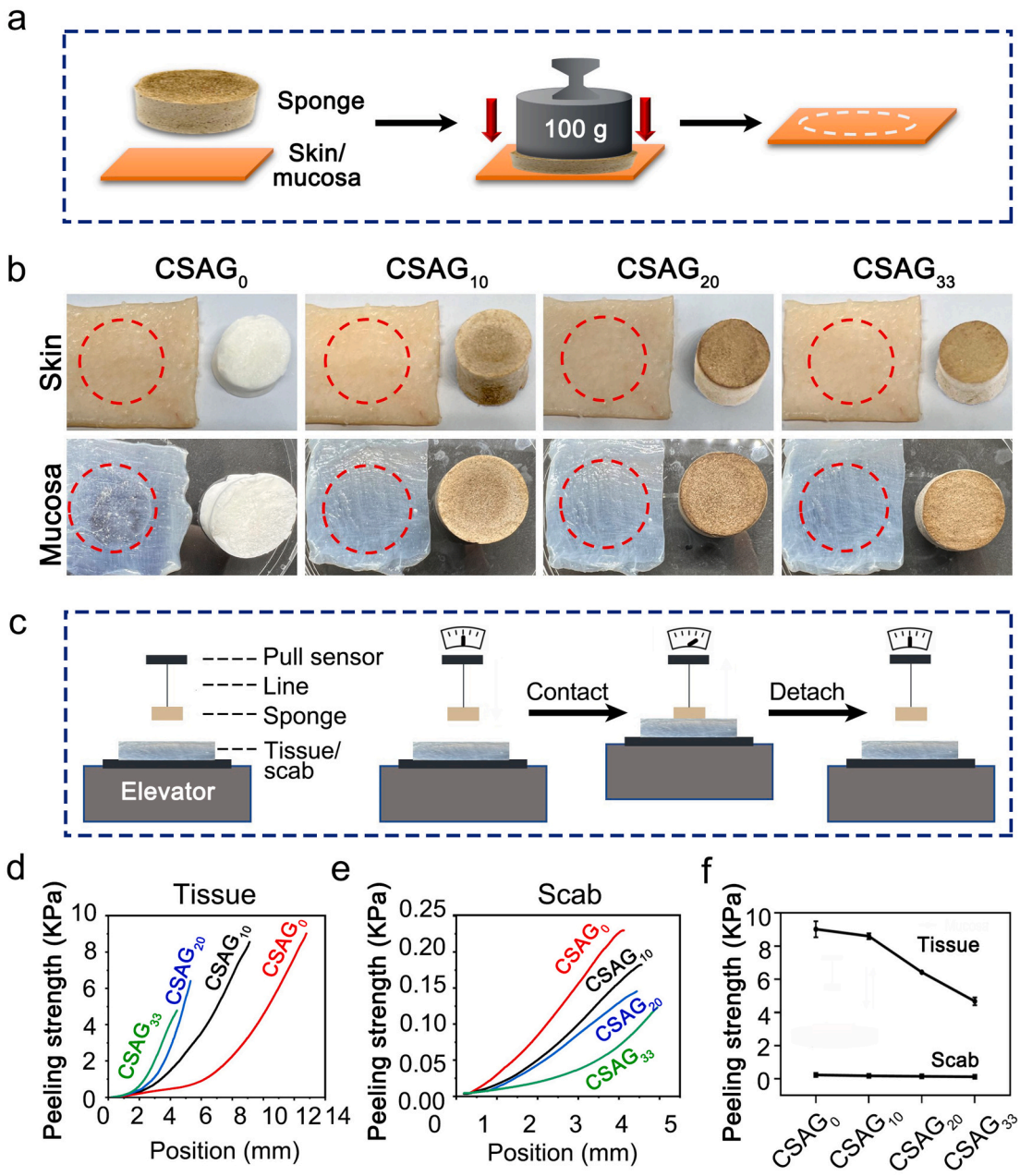

Fig. 6. *In vitro* anti-adhesion assays of CSAGs (a) Schematic diagram of adhesion test of CSAGs to porcine skin and porcine intestinal mucosa. (b) Photograph of porcine skin and mucosa after CSAGs peeling. (c) Schematic diagram of quantitative analysis of peeling strength between CSAGs and tissue/scab. Peeling strength of CSAGs against (d) tissue and (e) scab. (f) Comparison of the peeling strength of CSAGs on tissue and scab.

uneven, which might because of the presence of cavities at the interface between the material and the crust. All in all, $CSAG_{33}$ can safely be separated from the scabs to prevent secondary bleeding.

Based on the above results, we concluded that $CSAG_{33}$ effectively controlled serious hemorrhage without second bleeding because of its hydrophilic and anti-adhesion properties. Hydrophilicity was the fundamental property of $CSAG_{33}$ that accumulat red blood cells and platelets, triggered intrinsic/extrinsic coagulation stimulations, and formed a thick and stable blood scab to stop bleeding (Fig. 8a). Importantly, the low tissue adhesion and easy scab-separation contributed significantly to the safe peeling of $CSAG_{33}$ from the wound without re-bleeding (Fig. 8b).

For one thing, GO addition attenuated adhesion strength between CSAGs and tissue (Fig. 8b). The possible explanations were: i) GO addition weakened the interaction of $CSAG_{33}$ with tissue. There was electrostatic interaction between positively charged $CSAG_0$ and negatively charged sialic acid residues on tissue surface mucin (Hamedi et al., 2022; Wu et al., 2017), which was the leading cause of wound adhesion; while the addition of negative GO shielded the positive charge of $CSAG_{33}$ and significantly attenuated the electrostatic interaction force. Besides, the presence of the amino group in chitosan could form hydrogen bonding with different proteins and amino acids on the tissue surface (Mati-Baouche et al., 2014). The addition of GO depletes the positively charged amino group by curing reaction, which may weaken the hydrogen bond between $CSAG_{33}$ and tissue. ii) GO addition increased the porosity and surface roughness of $CSAG_{33}$. The porosity and roughness of the substrate surface have an important impact on tissue adhesion. When the rough surface comes into contacted with tissue, bubbles or cavities would be generated at the interface that effectively weakened their adhesion (Van der Leeden & Frens, 2002).

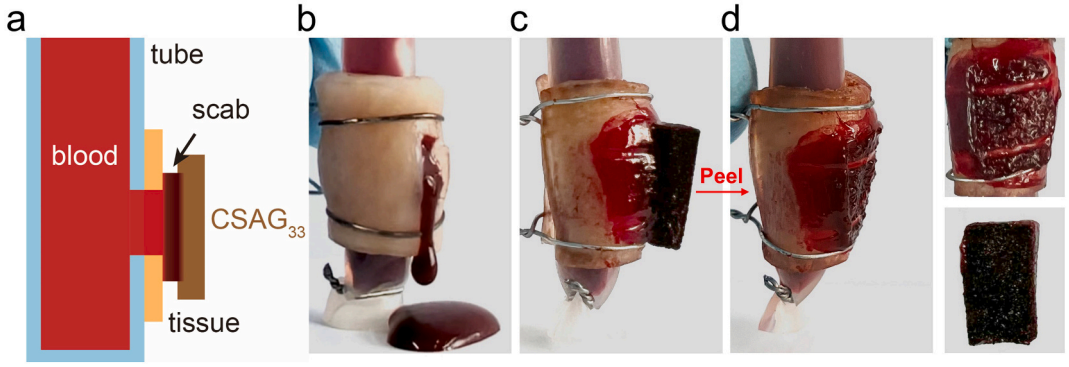

Fig. 7. Separation assays of material and scabs. (a) Schematic diagram of the peeling model. $CSAG_{33}$ was fixed by blood scabs to porcine skin wrapped in silicone tubing, a notch was created in the same place on the porcine skin and the silicone tube, blood was injected into a silicone tube and the $CSAG_{33}$ was carefully peeled from the blood scab. (b) Photograph of the blood being injected directly into the tube and (c) the tube blocked by the $CSAG_{33}$/scab composite. (d) Photograph of 'wound' and $CSAG_{33}$ after peeling.

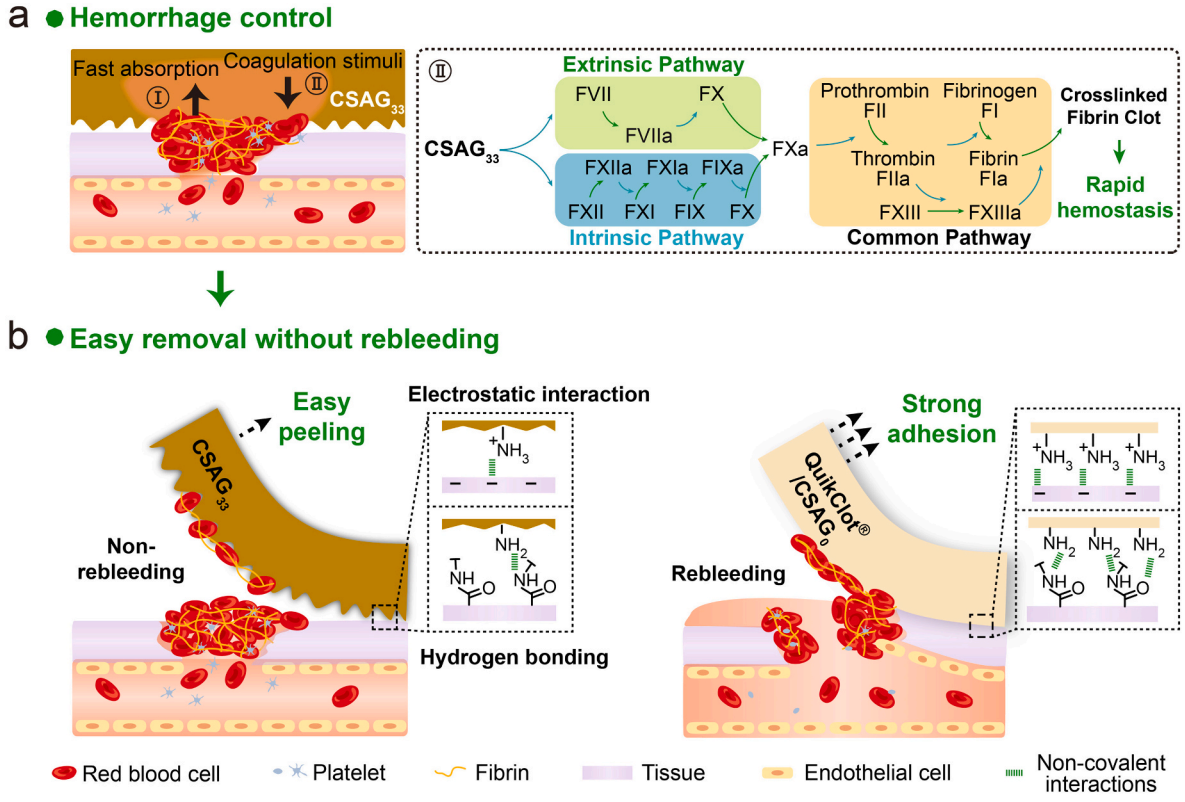

Fig. 8. Schematic diagram of hemostasis and anti-adhesion mechanism of $CSAG_{33}$. (a) First, the $CSAG_{33}$ rapidly absorbed plasma to enrich blood red blood cells and platelets for the rapid formation of primary clotting clots. Second, the $CSAG_{33}$ simultaneously activated exogenous and endogenous coagulation cascade pathways to reinforce the initial clotting plug through rich stimuli. (b) Compared to QuikClot® and $CSAG_0$, $CSAG_{33}$ exhibited weaker electrostatic interactions, hydrogen bonding interactions and higher porosity and surface roughness, which resulting in lower tissue adhesion strength. The removal of $CSAG_{33}$ was accompanied with the defect-driven detachment of part of the blood scab, which sustained the wound seal and achieved non-rebleeding removal. (For interpretation of the references to colour in this figure legend, the reader is referred to the web version of this article.)

Two-dimensional lamellar structure GO was compounded into a linear chitosan polymer network, which increased the porosity and roughness of $CSAG_{33}$ (Zhang et al., 2013). Consequently, $CSAG_{33}$ was easy to be peeled from the wounds by reducing electrostatic interaction, hydrogen bond interaction and increasing surface roughness.

For another, partial detachment of the $CSAG_{33}$/scab composite sustained the wound seal (Fig. 8b). Previous studies revealed that an intact blood clot is relatively stable, whereas it is easily torn when it acquires a defect. The defect will be further enlarged mechanically, leading to the clot detached along the peeling direction (Liu, Bao, Ma, Kastrup, & Li, 2021; Tutwiler et al., 2020). Consistently, high porosity and roughness $CSAG_{33}$ might introduce bubbles or cavities *i.e.* physical defects at the interface. As Fig. 7 and Fig. 8b illustrated, the scab could be gradually torn when the $CSAG_{33}$ was peeled off (also see Video S5). The resulted uneven surface between blood scab and $CSAG_{33}$ implied the existence of cavities. They could drive the transverse detachment of $CSAG_{33}$/scab composite in the presence of peeling force. As such, the removal of $CSAG_{33}$ would take away part of the blood scab (He et al., 2022), but most of the blood scab remained on wound to avoid re-bleeding.

Collectively, $CSAG_{33}$ was an effective anti-adherent hydrophilic

hemostatic sponge. First, $CSAG_{33}$ facilitated the formation of a high-density blood clot by hydrophilic interface stimulation. Second, $CSAG_{33}$ had low tissue adhesion because of its special physicochemical properties, which was critical to avoid wound tear by attenuating stripping force. Third, the subsequent removal of $CSAG_{33}$ was accompanied by the defect-driven partial detachment of the blood scab that sustained the wound seal.

4. Conclusions

In summary, we have firstly developed a series of hydrophilic CSAGs that effectively controlled serious hemorrhage without second bleeding. $CSAG_{33}$ with optimal GO addition (33 wt%) achieved rapid hemostasis under the synergetic effects of rapid absorption of plasma, large accumulation of red blood cells and platelets, and strong activation of intrinsic/extrinsic coagulation cascade. The hemostatic efficiency of $CSAG_{33}$ significantly outperformed that of the commercially available products CELOX™ and QuikClot® in two serious bleeding models *in vivo*. More importantly, $CSAG_{33}$ is effectively prevented wound adhesions, with a 79.3 % reduction in peeling force compared to the hemostatic gauze QuikClot® in a rat dorsal adhesion model. Anti-adhesion mechanism studies indicated that $CSAG_{33}$ has low tissue adhesion and defect-driven partial detachment of the blood scab, allowing $CSAG_{33}$ to be peeled easily and safely from the wound. Thus, we confirmed that $CSAG_{33}$ has great potential in rapid hemostasis and anti-adhesion for severe hemorrhage. This study develops a hydrophilic anti-adhesion hemostatic material and also provides new concepts for the design of anti-adhesive materials.

Supplementary data to this article can be found online at https://doi.org/10.1016/j.carbpol.2023.121058.

CRediT authorship contribution statement

Guofeng Li and Xing Wang: Design and interpretation of the study, Writing-Reviewing and Editing, Supervision, Project administration, Funding acquisition; **Fanglin Du:** Design of experiments, Materials preparation and evaluation, Animal experiment, Data curation, Writing-Original draft preparation; **Wenjing A** and **Fang Liu:** Assistance of animal experiments; **Bingxin Wu** and **Yichun Liu:** Assistance of coagulation tests; **Weitao Zheng:** Assistance of data analysis; **Wenli Feng:** Assistance of Writing and Reviewing of the paper.

Declaration of competing interest

The authors declare that they have no known competing financial interests or personal relationships that could have appeared to influence the work reported in this paper.

Data availability

The authors do not have permission to share data.

Acknowledgments

G. L. thanks the National Natural Science Foundation of China (22005020 and 22275013) for the financial support. G. L. thanks Guojun Zheng and Gaofei Hu from BUCT for the help of the NMR analysis.

References

Acik, M., Lee, G., Mattevi, C., Pirkle, A., Wallace, R. M., Chhowalla, M., … Chabal, Y. (2011). The role of oxygen during thermal reduction of graphene oxide studied by infrared absorption spectroscopy. *The Journal of Physical Chemistry C, 115*(40), 19761–19781.

Ariëns, R. A. (2016). Novel mechanisms that regulate clot structure/function. *Thrombosis Research, 141*, S25–S27.

Cines, D. B., Lebedeva, T., Nagaswami, C., Hayes, V., Massefski, W., Litvinov, R. I., … Weisel, J. W. (2014). Clot contraction: Compression of erythrocytes into tightly packed polyhedra and redistribution of platelets and fibrin. *Blood, 123*(10), 1596–1603.

Deineka, V., Sulaieva, O., Pernakov, N., Radwan-Pragłowska, J., Janus, L., Korniienko, V., Husak, Y., Yanovska, A., Liubchak, I., & Yusupova, A. (2021). Hemostatic performance and biocompatibility of chitosan-based agents in experimental parenchymal bleeding. *Materials Science and Engineering: C, 120*, Article 111740.

Depan, D., Girase, B., Shah, J., & Misra, R. (2011). Structure–process–property relationship of the polar graphene oxide-mediated cellular response and stimulated growth of osteoblasts on hybrid chitosan network structure nanocomposite scaffolds. *Acta Biomaterialia, 7*(9), 3432–3445.

Fang, Y., Xu, Y., Wang, Z., Zhou, W., Yan, L., Fan, X., & Liu, H. (2020). 3D porous chitin sponge with high absorbency, rapid shape recovery, and excellent antibacterial activities for noncompressible wound. *Chemical Engineering Journal, 388*, Article 124169.

Gulzar, A., Yang, P., He, F., Xu, J., Yang, D., Xu, L., & Jan, M. O. (2017). Bioapplications of graphene constructed functional nanomaterials. *Chemico-Biological Interactions, 262*, 69–89.

Guo, B., Dong, R., Liang, Y., & Li, M. (2021). Haemostatic materials for wound healing applications. *Nature Reviews Chemistry, 5*(11), 773–791.

Hamedi, H., Moradi, S., Hudson, S. M., Tonelli, A. E., & King, M. W. (2022). Chitosan based bioadhesives for biomedical applications: A review. *Carbohydrate Polymers, 119100*.

He, H., Zhou, W., Gao, J., Wang, F., Wang, S., Fang, Y., Gao, Y., Chen, W., Zhang, W., & Weng, Y. (2022). Efficient, biosafe and tissue adhesive hemostatic cotton gauze with controlled balance of hydrophilicity and hydrophobicity. *Nature Communications, 13*(1), 1–14.

Hegab, H. M., & Zou, L. (2015). Graphene oxide-assisted membranes: Fabrication and potential applications in desalination and water purification. *Journal of Membrane Science, 484*, 95–106.

Hong, Y., Zhou, F., Hua, Y., Zhang, X., Ni, C., Pan, D., … Lin, Q. (2019). A strongly adhesive hemostatic hydrogel for the repair of arterial and heart bleeds. *Nature Communications, 10*(1), 1–11.

Hu, Z., Zhang, D.-Y., Lu, S.-T., Li, P.-W., & Li, S.-D. (2018). Chitosan-based composite materials for prospective hemostatic applications. *Marine Drugs, 16*(8), 273.

Hummers, W. S., Jr., & Offeman, R. E. (1958). Preparation of graphitic oxide. *Journal of the American Chemical Society, 80*(6), 1339.

Jokinen, V., Kankuri, E., Hoshian, S., Franssila, S., & Ras, R. H. (2018). Superhydrophobic blood-repellent surfaces. *Advanced Materials, 30*(24), 1705104.

Klode, J., Schöttler, L., Stoffels, I., Körber, A., Schadendorf, D., & Dissemond, J. (2011). Investigation of adhesion of modern wound dressings: A comparative analysis of 56 different wound dressings. *Journal of the European Academy of Dermatology and Venereology, 25*(8), 933–939.

Kumari, S., Singh, M. K., Singh, S. K., Grácio, J. J., & Dash, D. (2014). Nanodiamonds activate blood platelets and induce thromboembolism. *Nanomedicine, 9*(3), 427–440.

Li, G., Quan, K., Liang, Y., Li, T., Yuan, Q., Tao, L., … Wang, X. (2016). Graphene-montmorillonite composite sponge for safe and effective hemostasis. *ACS Applied Materials & Interfaces, 8*(51), 35071–35080.

Li, G., Quan, K., Xu, C., Deng, B., & Wang, X. (2018a). Synergy in thrombin-graphene sponge for improved hemostatic efficacy and facile utilization. *Colloids and Surfaces B: Biointerfaces, 161*, 27–34.

Li, Y., Wang, X., Fu, Y.-n., Wei, Y., Zhao, L., & Tao, L. (2018b). Self-adapting hydrogel to improve the therapeutic effect in wound-healing. *ACS Applied Materials & Interfaces, 10*(31), 26046–26055.

Li, Z., Milionis, A., Zheng, Y., Yee, M., Codispoti, L., Tan, F., … Yap, C. H. (2019). Superhydrophobic hemostatic nanofiber composites for fast clotting and minimal adhesion. *Nature Communications, 10*(1), 1–11.

Li, J., Sun, X., Zhang, K., Yang, G., Mu, Y., Su, C., … Feng, C. (2020a). Chitosan/diatom-biosilica aerogel with controlled porous structure for rapid hemostasis. *Advanced Healthcare Materials, 9*(21), 2000951.

Li, X., Cheng, H., Huang, X., Li, S., Yang, R., Wang, J., & Wang, X. (2020b). Facile construction of chitin/graphene nanocomposite sponges for efficient hemostasis. *ACS Sustainable Chemistry Engineering, 8*(50), 18377–18385.

Li, Y., Niu, F., Zhao, X., Yap, C. H., & Li, Z. (2021). Nonwetting nanostructured hemostatic material for bleeding control with minimal adhesion. *Advanced Materials Interfaces, 8*(23), 2101412.

Liang, X., Chernysh, I., Purohit, P. K., & Weisel, J. W. (2017). Phase transitions during compression and decompression of clots from platelet-poor plasma, platelet-rich plasma and whole blood. *Acta Biomaterialia, 60*, 275–290.

Liang, Y., Xu, C., Liu, F., Du, S., Li, G., & Wang, X. (2019). Eliminating heat injury of zeolite in hemostasis via thermal conductivity of graphene sponge. *ACS Applied Materials & Interfaces, 11*(27), 23848–23857.

Liao, K.-H., Lin, Y.-S., Macosko, C. W., & Haynes, C. L. (2011). Cytotoxicity of graphene oxide and graphene in human erythrocytes and skin fibroblasts. *ACS Applied Materials & Interfaces, 3*(7), 2607–2615.

Liu, C., Zhang, D., He, Y., Zhao, X., & Bai, R. (2010). Modification of membrane surface for anti-biofouling performance: Effect of anti-adhesion and anti-bacteria approaches. *Journal of Membrane Science, 346*(1), 121–130.

Liu, J., Ye, L., Sun, Y., Hu, M., Chen, F., Wegner, S., … Butt, H. J. (2020). Elastic superhydrophobic and photocatalytic active films used as blood repellent dressing. *Advanced Materials, 32*(11), 1908008.

Liu, S., Bao, G., Ma, Z., Kastrup, C. J., & Li, J. (2021). Fracture mechanics of blood clots: Measurements of toughness and critical length scales. *Extreme Mechanics Letters, 48*, Article 101444.

Long, C., Qing, Y., Li, S., Cui, M., Han, M., An, K., Long, X., Liu, C., & Liu, C. (2021). Asymmetric composite wound nanodressing with superhydrophilic/superhydrophobic alternate pattern for reducing blood loss and adhesion. *Composites Part B: Engineering, 223*, Article 109134.

Lu, Z., Hanif, A., Sun, G., Liang, R., Parthasarathy, P., & Li, Z. (2018). Highly dispersed graphene oxide electrodeposited carbon fiber reinforced cement-based materials with enhanced mechanical properties. *Cement and Concrete Composites, 87*, 220–228.

Mati-Baouche, N., Elchinger, P.-H., de Baynast, H., Pierre, G., Delattre, C., & Michaud, P. (2014). Chitosan as an adhesive. *European Polymer Journal, 60*, 198–212.

Moradi, S., Hadjesfandiari, N., Toosi, S. F., Kizhakkedathu, J. N., & Hatzikiriakos, S. G. (2016). Effect of extreme wettability on platelet adhesion on metallic implants: From superhydrophilicity to superhydrophobicity. *ACS Applied Materials & Interfaces, 8*(27), 17631–17641.

Mosesson, M. W. (2005). Fibrinogen and fibrin structure and functions. *Journal of Thrombosis and Haemostasis, 3*(8), 1894–1904.

Nair, R., Wu, H., Jayaram, P., Grigorieva, I., & Geim, A. (2012). Unimpeded permeation of water through helium-leak–tight graphene-based membranes. *Science, 335*(6067), 442–444.

Quan, K., Li, G., Luan, D., Yuan, Q., Tao, L., & Wang, X. (2015). Black hemostatic sponge based on facile prepared cross-linked graphene. *Colloids and Surfaces B: Biointerfaces, 132*, 27–33.

Quan, K., Li, G., Tao, L., Xie, Q., Yuan, Q., & Wang, X. (2016). Diaminopropionic acid reinforced graphene sponge and its use for hemostasis. *ACS Applied Materials Interfaces, 8*(12), 7666–7673.

Reina, G., González-Domínguez, J. M., Criado, A., Vázquez, E., Bianco, A., & Prato, M. (2017). Promises, facts and challenges for graphene in biomedical applications. *Chemical Society Reviews, 46*(15), 4400–4416.

Ruhoff, A. M., Hong, J. K., Gao, L., Singh, J., Tran, C., Mackie, G., & Waterhouse, A. (2021). Biomaterial wettability affects fibrin clot structure and fibrinolysis. *Advanced Healthcare Materials, 10*(20), 2100988.

Singh, S. K., Singh, M. K., Nayak, M. K., Kumari, S., Shrivastava, S., Grácio, J. J., & Dash, D. (2011). Thrombus inducing property of atomically thin graphene oxide sheets. *ACS Nano, 5*(6), 4987–4996.

Song, F., Kong, Y., Shao, C., Cheng, Y., Lu, J., Tao, Y., Du, J., & Wang, H. (2021). Chitosan-based multifunctional flexible hemostatic bio-hydrogel. *Acta Biomaterialia, 136*, 170–183.

Tutwiler, V., Singh, J., Litvinov, R. I., Bassani, J. L., Purohit, P. K., & Weisel, J. W. (2020). Rupture of blood clots: Mechanics and pathophysiology. *Science Advances, 6*(35), eabc0496.

Uysal, M., Akbulut, H., Tokur, M., Algül, H., & Çetinkaya, T. (2016). Structural and sliding wear properties of Ag/Graphene/WC hybrid nanocomposites produced by electroless co-deposition. *Journal of Alloys and Compounds, 654*, 185–195.

Van der Leeden, M. C., & Frens, G. (2002). Surface properties of plastic materials in relation to their adhering performance. *Advanced Engineering Materials, 4*(5), 280–289.

Wang, C., Luo, W., Li, P., Li, S., Yang, Z., Hu, Z., … Ao, N. (2017). Preparation and evaluation of chitosan/alginate porous microspheres/Bletilla striata polysaccharide composite hemostatic sponges. *Carbohydrate Polymers, 174*, 432–442.

Wang, Y., Zhou, P., Xiao, D., Zhu, Y., Zhong, Y., Zhang, J., … Mao, Z. (2019). Chitosan-bound carboxymethylated cotton fabric and its application as wound dressing. *Carbohydrate Polymers, 221*, 202–208.

Wang, L., You, X., Dai, C., Tong, T., & Wu, J. (2020). Hemostatic nanotechnologies for external and internal hemorrhage management. *Biomaterials Science, 8*(16), 4396–4412.

Wang, Y., Lv, L., Liang, H., Liang, W., Chen, Z., Li, J., Liu, S., Hu, F., Zhu, J., & Liu, Q. (2022). Clot structure-based physical-matching design of platelet cloaking nano-delivery system facilitates specific arteriovenous thrombolysis. *Chemical Engineering Journal, 135982*.

Weisel, J. W., & Litvinov, R. I. (2017). Fibrin formation, structure and properties. In D. A. D. Parry, & J. M. Squire (Eds.), *Fibrous proteins: Structures and mechanisms* (pp. 405–456). Berlin: Springer International Publishing Inc.

Wenjing, A., Du, F., He, Y., Wu, B., Liu, F., Liu, Y., Zheng, W., Li, G., & Wang, X. (2022). Graphene oxide reinforced hemostasis of gelatin sponge in noncompressible hemorrhage via synergistic effects. *Colloids and Surfaces B: Biointerfaces, 220*, Article 112891.

Wu, W., Cheng, R., das Neves, J., Tang, J., Xiao, J., Ni, Q., Liu, X., Pan, G., Li, D., & Cui, W. (2017). Advances in biomaterials for preventing tissue adhesion. *Journal of Controlled Release, 261*, 318–336.

Wu, B., Du, F., Wenjing, A., Li, G., & Wang, X. (2022). Graphene-based hemostatic sponge. *Chinese Chemical Letters, 33*(2), 703–713.

Xie, H., Yu, Q., Mao, J., Wang, S., Hu, Y., & Guo, Z. (2020). A conductive polyacrylamide/double bond chitosan/polyaniline hydrogel for flexible sensing. *Journal of Materials Science: Materials in Electronics, 31*(13), 10381–10389.

Yan, X., Yang, J., Chen, F., Zhu, L., Tang, Z., Qin, G., … Chen, G. (2018). Mechanical properties of gelatin/polyacrylamide/graphene oxide nanocomposite double-network hydrogels. *Composites Science and Technology, 163*, 81–88.

Yang, X., Liu, W., Xi, G., Wang, M., Liang, B., Shi, Y., Feng, Y., Ren, X., & Shi, C. (2019). Fabricating antimicrobial peptide-immobilized starch sponges for hemorrhage control and antibacterial treatment. *Carbohydrate Polymers, 222*, Article 115012.

Yang, G., Wu, Y., Liu, M., Liang, J., Huang, Q., Dou, J., Wen, Y., Deng, F., Zhang, X., & Wei, Y. (2021). A novel method for the functionalization of graphene oxide with polyimidazole for highly efficient adsorptive removal of organic dyes. *Journal of Molecular Liquids, 339*, Article 116794.

Zhang, J., Xu, Z., Mai, W., Min, C., Zhou, B., Shan, M., Li, Y., Yang, C., Wang, Z., & Qian, X. (2013). Improved hydrophilicity, permeability, antifouling and mechanical performance of PVDF composite ultrafiltration membranes tailored by oxidized low-dimensional carbon nanomaterials. *Journal of Materials Chemistry A, 1*(9), 3101–3111.

Zhang, C., Yang, X., Hu, W., Han, X., Fan, L., & Tao, S. (2020). Preparation and characterization of carboxymethyl chitosan/collagen peptide/oxidized konjac composite hydrogel. *International Journal of Biological Macromolecules, 149*, 31–40.

Zhang, J., Jia, K., Huang, Y., Liu, X., Xu, Q., Wang, W., … Chen, H. (2021a). Intrinsic wettability in pristine graphene. *Advanced Materials, 2103620*.

Zhang, W., Wu, J., Yu, L., Chen, H., Li, D., Shi, C., … Fan, J. (2021b). Paraffin-coated hydrophobic hemostatic zeolite gauze for rapid coagulation with minimal adhesion. *ACS Applied Materials & Interfaces, 13*(44), 52174–52180.

Zhu, T., Wu, J., Zhao, N., Cai, C., Qian, Z., Si, F., … Shao, L. (2018). Superhydrophobic/superhydrophilic janus fabrics reducing blood loss. *Advanced Healthcare Materials, 7*(7), 1701086.